

Tuning Electronic Structure of 2D In_2S_3 via P Doping and Size Controlling Toward Efficient Photoelectrochemical Water Oxidation

Yuli Xiong, Lin Yang, Yan Zhu, Qingxin Lai, Ping Li, Peng Xiao,* and Guozhong Cao*

Two-dimensional (2D) lamellar materials possess the advantages of strong light-matter interactions and tunable band structure, rendering possible high conversion efficiency of solar to fuel. Herein, the controlled fabrication of small-sized P doped 2D In_2S_3 arrays (P- In_2S_3) via preseeding method is demonstrated, which is a feasible approach to regulate the bandgap and attain large specific surface area with more active sites. A fraction of S sites is substituted by P atoms to form In–P bonds, the substitutional doping introduces a hybridized state near the valence band of In_2S_3 through the integration of P 3s, P 3p, and S 3p orbitals. By P doping, the electronic structure is tuned, the charge recombination is suppressed, and the surface reaction kinetics are improved, addressing all three major problems at once for water oxidation. With the synergistic effect of size and impurity states, more than fivefold enhancement is achieved in photocurrent, and high oxidation kinetics efficiency (79%). Therefore, the combination of size controlling synthesis of a 2D lamellar structure and doping strategies can be further developed in solar energy conversion devices.

sluggish four electrons transfer process.^[4] Two-dimensional (2D) materials present the advantages of a short exciton diffusion distance and a thickness less than the width of the space charge region at solid/liquid interfaces, thus potentially serve as the excellent photoanodes.^[5,6] Indium sulfide (In_2S_3) is a broad-spectral 2D material with ordered vacancy spinel-like structure, the sulfide anions are closely packed in layers, with octahedral-coordinated In cations present within the layers, and tetrahedral-coordinated In cations between them.^[7,8] 2D In_2S_3 is an n-type semiconductor with small size effect, exhibiting large surface area when its size is of nanometers, exposing a high percentage of edges that could produce active surface toward catalytic reaction. The variation of size in nanometer scale could also tune the bandgap based on quantum size and surface effect.^[9,10]

1. Introduction

Photoelectrochemical (PEC) systems have been considered to be the promising and practical strategies for producing chemical fuels (e.g., H_2 from water splitting and hydrocarbons from CO_2 reduction), due to the low cost and energy consumption.^[1–3] In a complete PEC cycle, the water oxidation on photoanodes is more energetically demanding and rate limiting due to the


The common approaches to the fabrication of 2D In_2S_3 include chemical vapor deposition, hydrothermal, solvothermal, and sol-gel process, however, precise controlling the dimensions of this compound is still difficult and have not been reported.^[11,12] Fortunately, in a solvothermal reaction, the size and shape of the products could be controlled by nucleation and subsequent growth. The homogeneous nucleation limits the formation of nucleation sites and quantity attributing to the diversity of surface energy and nucleation barrier.^[13] In_2S_3 was fabricated by the former researchers usually leads to the large multilayer flakes,^[8,14] whereas a lower surface energy can make it easier to grow on seed sites. Therefore, seed-mediated growth has a good control of nucleation density, and thus attaining uniform structure with desired edges.

Introduction of alien atoms to 2D material is an effective way for tuning electrical and optical properties of the host material via orbital hybridization.^[15] The Fermi level E_F of most n-type semiconductors can be tuned by introducing impurity doping which is capable of causing dramatic changes in their interlayer electrical structure.^[16–18] Once the position of hybridized impurity level is near the E_F or valence band, it becomes the electrons or holes trap center (e.g., P-CdS and Gd-BiVO₄) and then affects the charge separation.^[19–21] The doping pattern of the impurity species in the host materials include interstitial and substitutional sites. If an impurity atom is located in the gap between atoms in the lattice, it often refers to an interstitial doping, whereas an impurity atom substitute at the position of metal or chalcogen

Y. Xiong, Dr. L. Yang, Y. Zhu, Prof. P. Xiao
Chongqing Key Laboratory of Soft Condensed Matter Physics
and Smart Materials
College of Physics
Chongqing University
Chongqing 400030, China
E-mail: xiaopeng@cqu.edu.cn

Q. Lai, P. Li
College of Chemistry and Chemical Engineering
Chongqing University
Chongqing 400030, China

Prof. G. Cao
Department of Materials Science and Engineering
University of Washington
Seattle WA98195, USA
E-mail: gzcao@u.washington.edu

 The ORCID identification number(s) for the author(s) of this article can be found under <https://doi.org/10.1002/solr.202000618>.

DOI: 10.1002/solr.202000618

site, which defined as substitutional doping. Substitutional doping involves the chemical bonding (usually covalent) between dopant atoms and host lattice, it is stably to tune the electrical, magnetic, and catalytic properties compared with metastable surface charge transfer processes (interstitial doping).^[22] For instance, substitutional Nb doping in MoS₂ could induce a crystal conversion from 2H to 3R stacking in the layered structure attribute to the changes in *d*-electron, forming an impurity state near the host valence band and promoting the carriers' mobility.^[23] Substitutional Mo sites by Re in monolayer MoS₂ demonstrated a 0.5 eV shift of *E_F* toward the conduction band, resulting in a degeneration of n-type donor and reduced the sulfur deficiency simultaneously.^[24] Despite there has some relevant works on band engineering by doping semiconductors, the influence of substitutional doping triggered on charge redistribution and interaction during PEC process has not been well addressed.^[19,25,26]

Herein, motivated from the aforementioned studies, we regulated the growth of 2D In₂S₃ arrays to a smaller size (In₂S₃(s)) by preseeding method, followed by a solvothermal process. The In₂S₃(s) presents a larger specific surface area with more active sites, also tuning the band structure at nanometer scale. Further, as a result of substitution of S position by P dopant, the hybridized state (In–P structure) was formed near the valence band thanks to the integration of P 3s, 3p, and S 3p orbitals. This hybridized state could broaden the depletion width, bend the energy band upward, and accelerate the hole's transfer to surface. Combined with the effects of size and impurity states, the photocurrent was enhanced by 5.3-fold for 2D P-In₂S₃(s) compared with In₂S₃. In a nutshell, the charge transfer dynamics were systematically studied in the context of light absorption, charge

separation, and surface reaction with an experimental and theoretical approaches.

2. Results and Discussion

The synthesis of P-In₂S₃(s) nanosheet arrays involves three steps, as shown in Figure 1a: First, the In₂S₃ seed layer was grown on the fluorine-doped tin oxide (FTO) substrate by succession ionic layer adsorption reaction (SILAR) method, where surface coagulation occurred around these nucleation sites (Figure S1, Supporting Information). The reaction during SILAR process is given as: $2\text{In}^{3+} + 3\text{S}^{2-} \rightarrow \text{In}_2\text{S}_3$. Second, the seed layer was used as the substrate to fabricate small-sized In₂S₃(s) arrays by solvothermal route, which yields small-sized 2D nanosheets. Third, the In₂S₃(s) film was placed into a tube furnace for phosphorizing and the final products of 2D P-In₂S₃(s) arrays was obtained. X-ray diffraction (XRD) pattern (Figure 1b) suggests that the sample has a typical tetragonal In₂S₃ structure (25-0390).^[27] The diffraction peaks at 27.43°, 33.23°, and 47.70° are readily indexed to the (109), (0012), and (2212) crystal planes for pristine In₂S₃. However, a detailed inspection of the main diffraction peaks reveals the peaks in P-In₂S₃(s) is shifted slightly toward to a lower 2θ , the angle peaks' location is higher, the shift is larger. Especially the interplanar space corresponding to (2212) crystal plane of pristine In₂S₃ is estimated to be 1.90 Å from the XRD pattern, whereas the diffraction peak of P-In₂S₃(s) shifts to a lower 2θ by 0.5° at this crystal plane, implying the interplanar space increased by 0.02 Å. This phenomenon evidenced the S position has been replaced by P atom and the ionic radius of P is bigger than that of S.^[20] The In₂S₃ seeds have a very small size and a poor crystallinity, the diffraction peaks of P_n-In₂S₃(s)

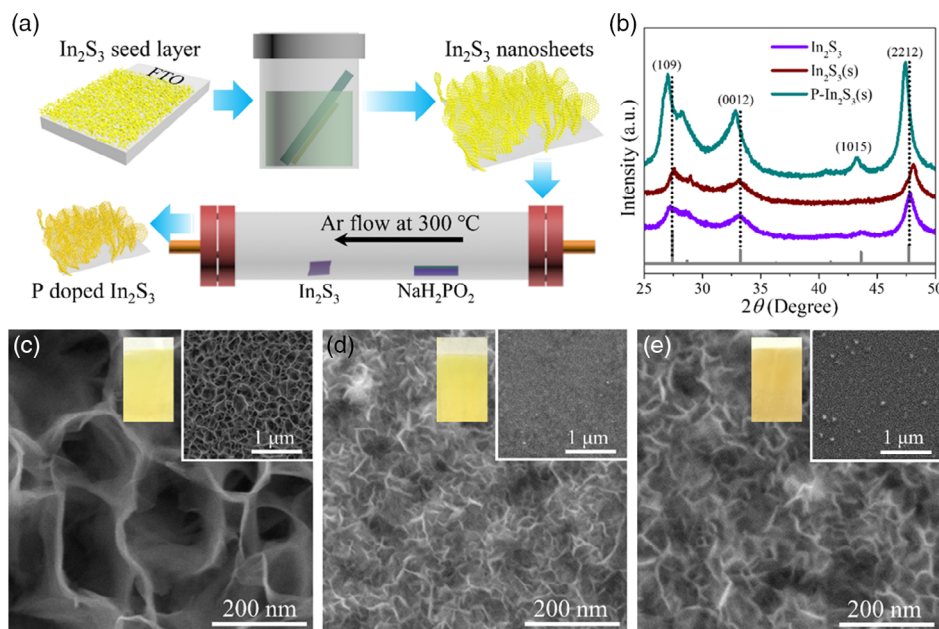


Figure 1. Fabrication of 2D In₂S₃ arrays and morphologies. a) The synthetic of P-In₂S₃(s) involves three steps: preseeding, solvothermal, and CVD doping process. b) The XRD pattern of different 2D In₂S₃ arrays scraped from FTO substrate. The top view morphologies of the as-prepared samples, including the SEM of c) In₂S₃, d) In₂S₃(s), and e) P-In₂S₃(s), insets indicate the uniform and highly coverage characteristic in low magnified view, and the optical photographs of these films.

(n represents the phosphorizing time) shift more toward lower angle, with increased phosphating time (Figure S2, Supporting Information). The scanning electron microscopy (SEM) image in Figure 1c depicts the 2D In_2S_3 nanosheet arrays were grown perpendicularly to the FTO substrate. These nanosheets with a diameter of approximately 150 nm and a thickness of 10 nm are interconnected to form a honeycomb-like morphology, and the film's thickness is ≈ 800 nm. However, for the sample grown on the seed layer, $\text{In}_2\text{S}_3(\text{s})$ arrays display a denser morphology compared with In_2S_3 in one-step growth (Figure 1d and Figure S3, Supporting Information). The thickness of $\text{In}_2\text{S}_3(\text{s})$ is stacked by multilayers, and the size of all nanosheets has decreased to ≈ 20 nm, both the optical photographs of the two films have the yellow color in macroscopic scale. The 2D $\text{P-In}_2\text{S}_3(\text{s})$ arrays retain similar morphologies of pristine $\text{In}_2\text{S}_3(\text{s})$, indicating the phosphorizing treatment did not affect the structure (Figure 1e). In addition, the inset figure reflects the homogeneous nanosheets grown on the substrate, whereas the optical photograph of the P-doped film presents a darker yellow color due to the slight changes in its crystal structure.

Moreover, the transmission electron microscopy (TEM) image illustrates the aggregated nanosheets morphology has a thin wrinkled-paper-like structure, the radial size of pristine In_2S_3 (150 nm) is in congruent with the SEM image (Figure 2a). Nevertheless, the curled morphology of seeded $\text{In}_2\text{S}_3(\text{s})$ describes a thinner nanosheet structure, and the radial size is dramatically decreased to ≈ 20 nm (Figure 2b and Figure S4, Supporting Information). The seed-stimulated heterogeneous nucleation

cuts off the edges extending, leading to more than 7 times shrink in the nanosheets attribute to the inadequate growth energy. The TEM image of $\text{P-In}_2\text{S}_3(\text{s})$ and $\text{In}_2\text{S}_3(\text{s})$ is comparable both in its size and lamellar structure (Figure 2c), the evidence that P doping in surface cannot change the morphologies. From the elemental mappings results, the bright color of In and S atoms are located in the backbone region but P atoms are dimmer, that is, the P are doped into the whole nanosheets by a nonmetal termination feature.^[28] According to the sectional TEM view, the thickness of $\text{In}_2\text{S}_3(\text{s})$ and $\text{P-In}_2\text{S}_3(\text{s})$ single nanosheet is ≈ 10 nm, verifying the nanosheet is just composed by 10–12 layers (Figure S5, Supporting Information). The EDS line scan across $\text{P-In}_2\text{S}_3(\text{s})$ demonstrates that In and S signals are mostly detected from the sheet regions, whereas the P element intensity is the lowest, proving a trace of P in the host material again (Figure S6, Supporting Information). To obtain the quantity of P in the $\text{P-In}_2\text{S}_3(\text{s})$ hybrid structure, the inductively coupled plasma (ICP) tests were conducted. The results display the content of P in $\text{P}_{10}\text{-In}_2\text{S}_3(\text{s})$ is $\approx 4.6\%$, and the amount of P is increasing as the phosphorizing time (Table S1, Supporting Information). Under the phosphorizing process, the PH_3 gas as the source of P dopants could be rapidly decomposed from sodium hypophosphite, the S element in In_2S_3 forms H_2S gas and then let out. In addition, the 3.79 Å lattice fringe distance (d-spacing) for (116) plane was observed by high resolution TEM (Figure 2d,e) both in In_2S_3 and $\text{In}_2\text{S}_3(\text{s})$, identifying the two samples has a similar crystal structure except for the size. However, doping P species into $\text{In}_2\text{S}_3(\text{s})$ will lead to the increases

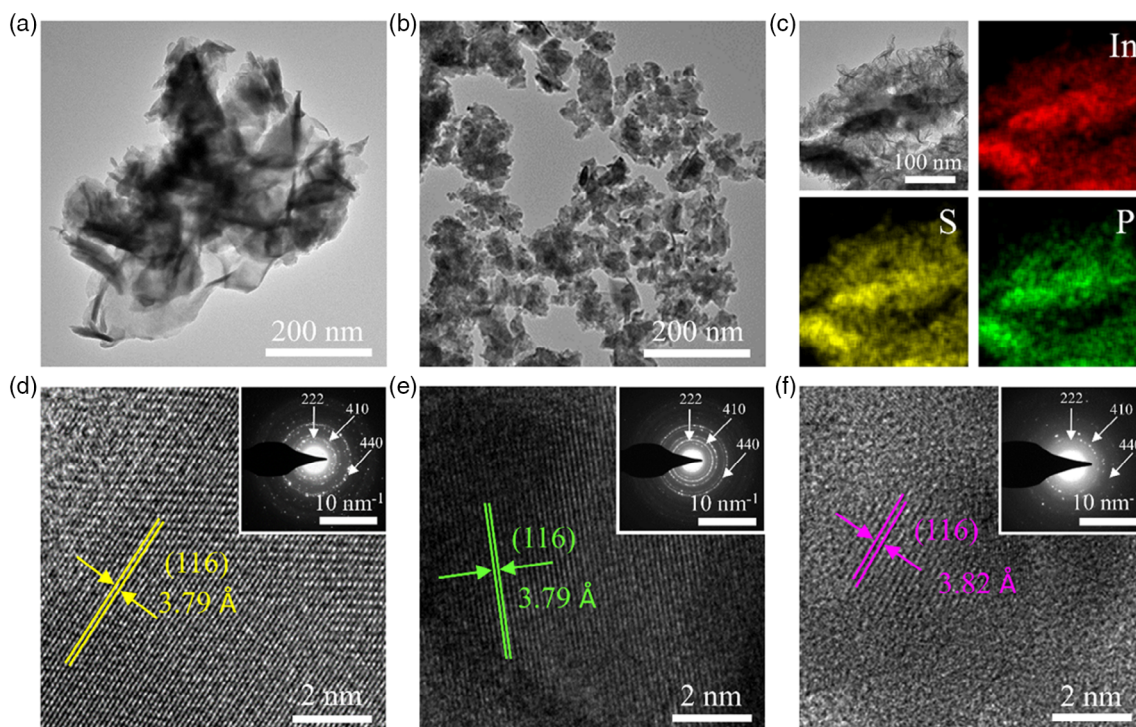


Figure 2. The microstructural features of different In_2S_3 nanosheets. The TEM image of a) In_2S_3 nanosheet and b) $\text{In}_2\text{S}_3(\text{s})$ nanosheet. c) TEM image of $\text{P-In}_2\text{S}_3(\text{s})$ and the corresponding elemental mappings, showing the distribution of In, S, and P elements. The high-resolution TEM lattice fringes of d) In_2S_3 , e) $\text{In}_2\text{S}_3(\text{s})$, and f) $\text{P-In}_2\text{S}_3(\text{s})$ crystal structure, with the indicated crystal plane spacing. These insets are the well-matched selected-area electron diffraction patterns of samples.

in lattice constant (3.82 Å) slightly (Figure 2f).^[29] The changed lattice constant by P-In₂S₃(s) corroborates to the XRD diffraction peak's shifting, the bigger atomic radius of P induces the 0.03 Å crystal plane distance expands. The selected area electron diffraction (SAED) pattern with obvious polycrystalline rings makes known the In₂S₃(s) nanosheets are composed of nanocrystals.^[30] Due to the larger lattice constant of P-In₂S₃(s) compared with In₂S₃, the SAED pattern depicts the blurry polycrystalline rings.

For the surface information, X-ray photoelectron spectroscopy (XPS) spectrum proves the In 3d and S 2p for P-In₂S₃(s) shifted positively by 0.4 eV in contrast to In₂S₃(s), implying a fraction of S sites have been substituted by P atoms to form In–P bonds (Figure S7, Supporting Information).^[24,31] The P 2p peaks point out the presence of P in 3-oxidation state by InP structure, and part of PO₄³⁻ oxidation state originates from the oxidized surface during exposing the nanosheets into air.^[25,32] Raman bands of In₂S₃(s) were observed at 131, 180, 250, 305, and 363 cm⁻¹, whereas these peaks in P-In₂S₃(s) are shifted to a higher frequency, a decrease in the In–S band length is detected, in other words, the In–P structure instead of the In–S.^[33] This result illustrates the distortion of In–S in In₂S₃(s) by the P³⁻ in InP, the P has been incorporated into the lattice through substitution of S is indicated. Thermogravimetric analysis (TGA) at atmospheric pressure of N₂ (Figure S8, Supporting Information) reveals the existence of phosphorous; the 2.2% weight loss below 200 °C is mainly attributed to the loss of free water in In₂S₃(s) and P-In₂S₃(s). In the temperature range of 600–900 °C, the weight loss of P-In₂S₃(s) (1.5%) is less than In₂S₃(s) (3.1%), testifying the In–P structure will influence the pyrolysis process and make the host material more stable below 900 °C.

To shed light on how the In–P species affect the PEC water splitting, the water oxidation reaction was investigated by a typical current–potential (*J*–*V*) measurement in a three-electrode system under neutral solution. The geometric surface area of all photoanodes was maintained at 1 cm² by a Teflon polymer gasket (inset of Figure 3a), and these films were all illuminated from the front direction. For In₂S₃(s), the photocurrent reaches a value of 0.3 mA cm⁻² at 1.23 V versus reversible hydrogen electrode (RHE), but the photocurrent of In₂S₃ is just 0.15 mA cm⁻²,

much lower than In₂S₃(s) (Figure 3a). The twofold enhancement in photocurrent interprets the size effect and the large specific surface area is beneficial for water oxidation in solution. Obviously, 2D P-In₂S₃(s) demonstrates the improved photocurrent of 0.8 mA cm⁻² at 1.23 V versus RHE, in comparison with 5.3-fold enhancement to pristine In₂S₃, exhibiting the In–P structure can reinforce the charge transfer dynamics significantly. Figure S9, Supporting Information, displays the chopped photocurrent of P-In₂S₃(s) arrays with various phosphorizing time, and the highest photocurrent was obtained by phosphorizing 10 min. This phenomenon can be explained that the short phosphorizing time cannot induce adequate impurely state toward charge separation, whereas longer treatment will cause additional recombination center. The 150 mV cathodic shift of onset photocurrent is observed in P-In₂S₃(s) compared with In₂S₃(s), implying P-doping raised the *E_F* and lowered the energy barrier through tuning the electronic structure.^[34] Electrochemical surface area (ECSA) measured are 8.3, 16.3, and 22.2 cm² for In₂S₃, In₂S₃(s), and P-In₂S₃(s), respectively, as shown in Figure S10, Supporting Information. The reduced nanosheet size causes the twofold increase in ECSA by In₂S₃(s), which is consistent with the photocurrent doubling.^[26] Figure 3b delivers the ECSA-normalized photocurrent densities (*J_{ECSA}*) of In₂S₃ (0.016 mA cm⁻² ECSA⁻²) and In₂S₃(s) (0.019 mA cm⁻² ECSA⁻²) at 1.23 V versus RHE. The *J_{ECSA}* values reflect the intrinsic catalytic activity, based on the active sites density, which is independent with the size of the sample. Instead *J_{ECSA}* of P-In₂S₃(s) suggests a significant improvement of water oxidation due to the more active sites generated by P doping. The twofold enhanced *J_{ECSA}* (0.036 mA cm⁻²) by P-In₂S₃(s) illustrates the energetic intrinsic electrochemically active, and even higher than some of the other relevant works (Table S2, Supporting Information).

The UV–vis absorption spectra (Figure 4a) shows a greater light absorption of In₂S₃(s) in the region of <500 nm due to the size confinement in nanosheets, similar to the reported results.^[35] Further, the electronic band structure of the small-sized In₂S₃(s) was tailored and made the bandgap narrowed after substitutional P doping, the film displays a

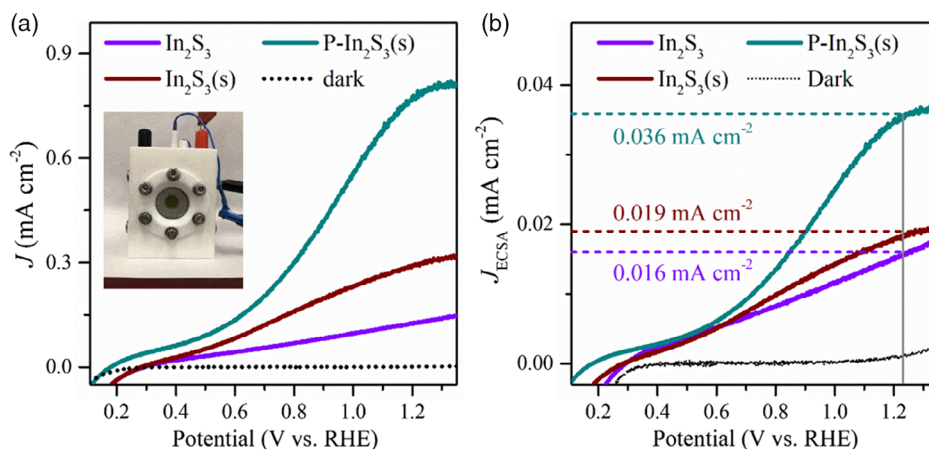


Figure 3. PEC performances of as-prepared 2D In₂S₃-based photoanodes for water oxidation. a) *J*–*V* plots of different photoanodes measured under AM 1.5G illumination (100 mW cm⁻²) for water oxidation; inset is the PEC physical setup. b) ECSA normalized photocurrent density for In₂S₃, In₂S₃(s), and P-In₂S₃(s) photoanodes.

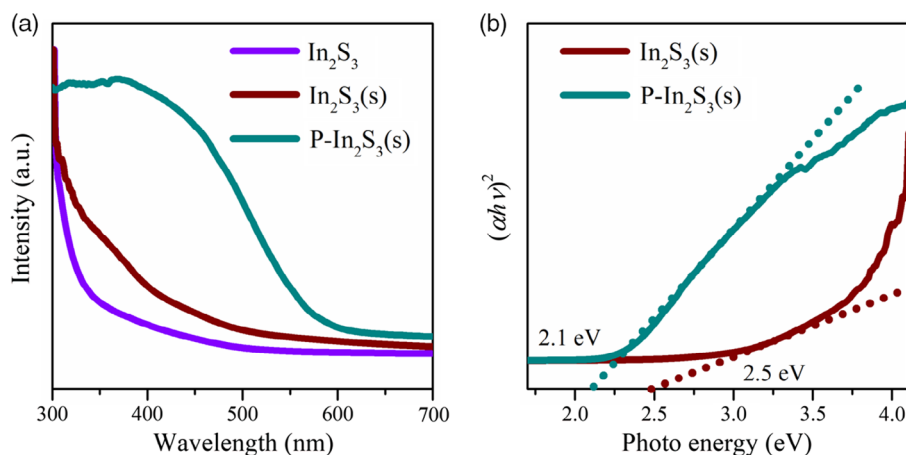


Figure 4. Optical features and band structures of as-prepared samples. a) The UV-vis absorption spectra of In_2S_3 , $\text{In}_2\text{S}_3(\text{s})$, and $\text{P-In}_2\text{S}_3(\text{s})$, and b) the corresponding bandgap evaluation from the plot of $(\alpha h\nu)^2$ versus the absorbed photon energy ($h\nu$).

dramatically photo-absorption increase between 400 and 600 nm, as the bandgap shrank to 2.1 eV (Figure 4b). The reduction of bandgap by P doping could be attributed to the constitution of localized impurity states in the bandgap region, eliciting more excited electrons through the interaction of electronic structure.^[30] Density functional theory (DFT) calculation suggests the direct bandgap in $\text{In}_2\text{S}_3(\text{s})$ converts to indirect bandgap in $\text{P-In}_2\text{S}_3(\text{s})$, this phenomenon could be explained that the In–P induces an impurity state into their bandgap (Figure S11, Supporting Information). Thus, the transition of an electron from the valence band to conduction band would undergo a relaxation process, and the direct recombination of photogenerated electron–hole pair is inhibited. However, it is noteworthy that the description of exchange-correlation effects utilizes the general gradient approximation (GGA), which tends to lead to an underestimation of bandgaps, resulting in a deviation from actual experimental conditions.^[31]

The photogenerated electron–hole separation efficiency (η_{sep}) as a function of applied potential was calculated and shown in Figure 5a and Figure S12, Supporting Information; the lower η_{sep} of In_2S_3 and $\text{In}_2\text{S}_3(\text{s})$ describes the large charge recombination is occurred. Whereas $\text{P-In}_2\text{S}_3(\text{s})$ exhibits the η_{sep} is 40% at 1.23 V versus RHE, manifests 2.2 and 1.5 times higher than In_2S_3 and $\text{In}_2\text{S}_3(\text{s})$, unfolding the In–P structure can promote the charge separation. Mott–Schottky (M–S) plots for all samples clarify that they are belonging to n-type semiconductors, and the flat band potential (V_{fb}) of In_2S_3 and $\text{In}_2\text{S}_3(\text{s})$ are 0.14 and 0.07 V versus RHE (Figure 5b), respectively. Nevertheless, the V_{fb} of $\text{P-In}_2\text{S}_3(\text{s})$ is negatively shifted by 120 mV, corresponding well with the negative shift of onset photocurrent, which demonstrates the hybridized states can upshift the band structure and reduce the energy barrier for water oxidation. Typically, the bottom of conduction band in n-type semiconductor is approximately more negative by 0.2 V than the V_{fb} , and therefore the upshifted E_{F} by $\text{P-In}_2\text{S}_3(\text{s})$ is beneficial for transferring the holes to surface where water oxidation takes place (Figure S13, Supporting Information).^[36] The carrier concentration N_{d} of these samples was estimated by fitting the M–S equation at the linear region; the N_{d} of In_2S_3 , $\text{In}_2\text{S}_3(\text{s})$, and $\text{P-In}_2\text{S}_3(\text{s})$ are found to be

1.2×10^{28} , 2.1×10^{28} , and $6.0 \times 10^{28} \text{ cm}^{-3}$.^[26] The nearly 3 times of N_{d} for $\text{P-In}_2\text{S}_3(\text{s})$ suggest the hybridized state can raise its conductivity, and enhance the charge transfer, as expected. In addition, the photovoltage (V_{ph}) was determined by measuring the changes of the surface potential (V) before and after illumination, which can be written as: $V_{\text{ph}} = |V_{\text{dark}} - V_{\text{light}}|$. The largest V_{ph} ($\approx 650 \text{ mV}$) in $\text{P-In}_2\text{S}_3(\text{s})$ announces the quasi-Fermi level of holes shifts downward and more holes can be dragged to the surface, reflecting a stronger charge transfer dynamics (Figure 5c). Next, the charge transport and recombination properties were investigated to understand the influence of P substitution doping by controlled intensity modulated photocurrent spectrometer (CIMPS). Figure 5d and Figure S14, Supporting Information, unfold the electrons transport time τ from the surface of photoanode to the FTO substrate, the $\text{P-In}_2\text{S}_3(\text{s})$ possesses the shortest transport time of 1.6 μs during water oxidation under illumination. The fast charge transport time is dominating the chemical reaction kinetics, affirming the P doping can promote the charge separation and improve the capability of carriers' migration, as identified by the high photocurrent.

Photoluminescence (PL) spectra of $\text{In}_2\text{S}_3(\text{s})$ and $\text{P-In}_2\text{S}_3(\text{s})$ arrays reveal a relatively uniform PL emission with two main emission bands at 561 and 587 nm,^[20,37] the emission at 561 nm is attributed to a band-to-band transition, whereas the low-energy emission at 587 nm can be assigned to deep-level interstitial site and defects (Figure 5e). In contrast, the weak PL intensity of $\text{P-In}_2\text{S}_3(\text{s})$ suggests a lower recombination rate of carriers. The hybridized state by P doping could behave as the charge traps to suppress charge recombination because the electrons in the traps will take a long time for exciting to conduction band, resulting in an efficient charge separation.^[38] Figure 5f shows the spectra of time-resolved transient PL (TRPL) decay, the plot on semiology scale shows the third-order exponential decay (Table S3, Supporting Information).^[20,39] The fitted time profiles imply the $\text{P-In}_2\text{S}_3(\text{s})$ has a longer decay time (681.1 ps) than $\text{In}_2\text{S}_3(\text{s})$ (665.9 ps), proving the impurity states are effective in prolonging the lifetime of photogenerated electrons hence facilitating the charge transport from the conduction band of $\text{P-In}_2\text{S}_3(\text{s})$ to FTO substrate. These results reflect a decrease in

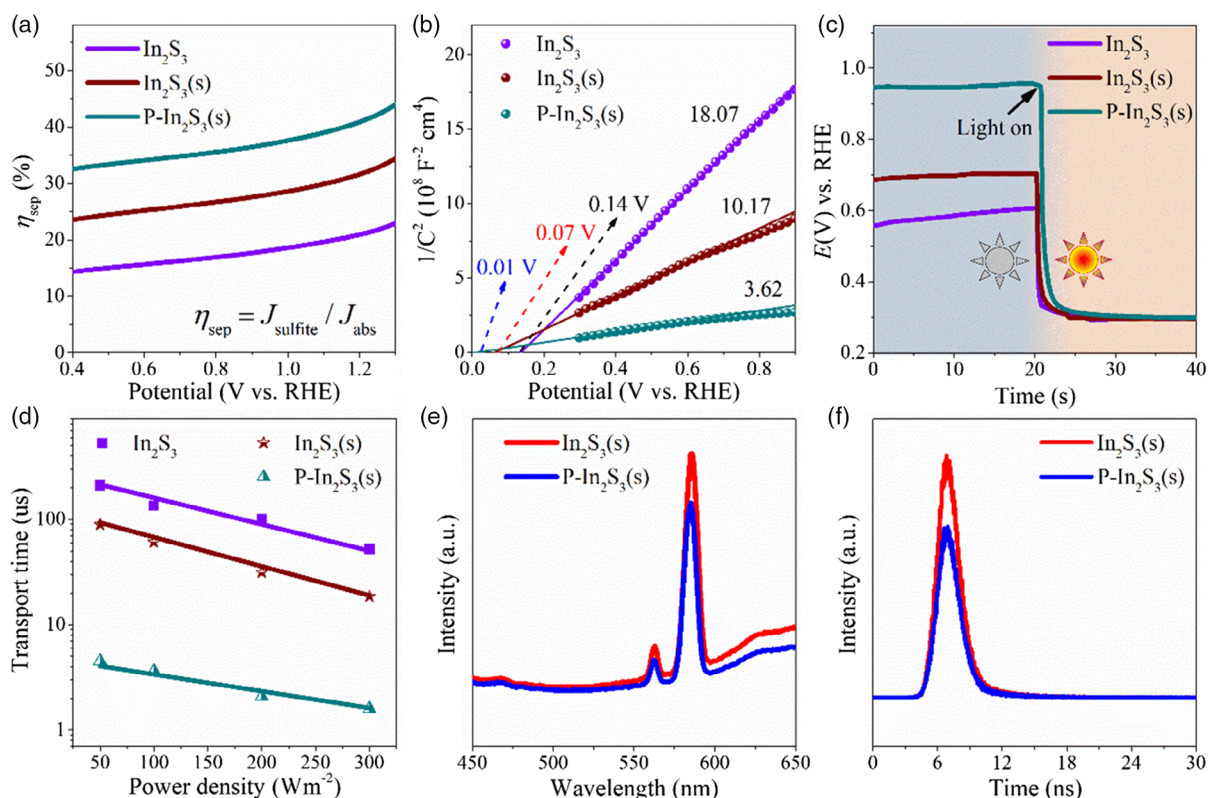


Figure 5. Charge separation and transfer kinetics characteristics of different In_2S_3 -based photoanodes with water oxidation. a) The efficiency of charge separation of these photoanodes. b) Mott–Schottky curves of In_2S_3 , $\text{In}_2\text{S}_3(\text{s})$, and $\text{P-In}_2\text{S}_3(\text{s})$ in $0.2\text{ M Na}_2\text{SO}_4$ solution with the frequency of 1000 Hz in dark. c) The photovoltage changes for various photoanodes in $0.2\text{ M Na}_2\text{SO}_4$ solution under light/dark condition, and d) charge transport time τ originated from CIMPS Nyquist plot at 1.23 V versus RHE under different light intensities ($\lambda = 365\text{ nm}$). e) PL spectra and f) TRPL decay of $\text{In}_2\text{S}_3(\text{s})$ and $\text{P-In}_2\text{S}_3(\text{s})$.

radiative recombination under the help of In–P structure considering the fact that Auger recombination is negative.^[40]

To understand the surface chemical reaction after P doping, the charge oxidation kinetics η_{oxi} represents the quantity of holes involved in the water oxidation (investigated by CIMPS). The increased η_{oxi} of $\text{In}_2\text{S}_3(\text{s})$ describes an increase in hole injection efficiency, attributed to the more surface active sites are exposed

due to the smaller size of nanosheets, significantly boosting the catalytic reactivity (Figure 6a).^[10] The η_{oxi} of $\text{P-In}_2\text{S}_3(\text{s})$ is vastly improved throughout the whole potential window, i.e., η_{oxi} reaches 79% at 1.23 V versus RHE, displaying 3.3 and 2.0 times higher than In_2S_3 and $\text{In}_2\text{S}_3(\text{s})$. This result illustrates the In–P hybridization could boost hole transfer to the interface between semiconductor and liquid, and matched well with the prolonged

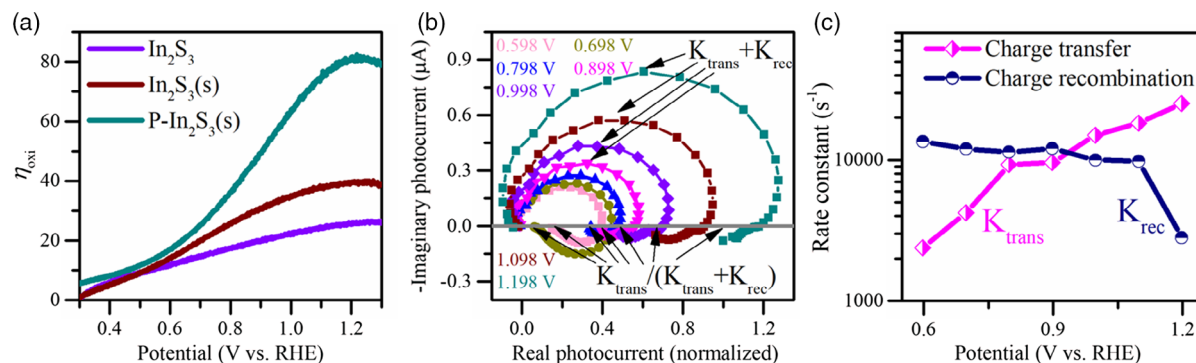


Figure 6. Charge injection and oxidation kinetics of different samples at photoanode/electrolyte interface for water oxidation. a) The efficiency of charge oxidation kinetics of these photoanodes. b) CIMPS–Nyquist plot of $\text{P-In}_2\text{S}_3(\text{s})$, the imaginary photocurrent versus the real photocurrent at different applied potentials. Arrows represent the charge transfer rate constant (K_{trans}) and charge recombination rate constant (K_{rec}). c) A total of 5% of the light is modulated from 100 kHz down to 0.1 Hz , whereas the K_{trans} and K_{rec} are extracted from the CIMPS data.

lifetime of photogenerated electrons. Moreover, analysis of the frequency-dependent CIMPS response gives deeply information about the competition of electron-hole's recombination and transfer at photoanode/electrolyte interface.^[41,42] Figure 6b shows a Nyquist complex photocurrent of P-In₂S₃(s) at various applied potentials, where K_{trans} and K_{rec} are the surface charge transfer and recombination rate constants. In this plot, the low-frequency intercept of real photocurrents indicates the charge transfer efficiency $K_{\text{trans}}/(K_{\text{trans}} + K_{\text{rec}})$. The rate constants at the apex of the semicircle, where the maximum phase shift is measured, representing the combined rate of charge transfer and recombination ($K_{\text{trans}} + K_{\text{rec}}$) (Figure S15, Supporting Information). With the potential moves positively, these plots trend to an increased charge transfer rates whilst the rate constant of recombination decreases (Figure 6c). The calculated K_{trans} of P-In₂S₃ is 8.9 times as the constant of K_{rec} (2812 s^{-1}) at 1.198 V versus RHE. Compared with In₂S₃, the K_{trans} of P-In₂S₃(s) is higher and the K_{rec} is lower, both of which certifies the In-P structure is beneficial for enhancing PEC reaction (Figure S16, Supporting Information). Ascribed to the dual role of P-In₂S₃(s) photoanode, charges' recombination at surface is reduced, particularly in >0.9 V versus RHE, corresponding well with highly photocurrent at 1.23 V versus RHE. Consistently, the P-In₂S₃(s) shows a better PEC performance compared with In₂S₃ and In₂S₃(s), which is summarized in Table S4, Supporting Information.

Figure 7a shows the surface potential of In₂S₃(s) measured using Kelvin probe force microscopy (KPFM), a bright region corresponds to a higher surface potential, whereas the dark region signifies a lower surface potential.^[43] For P-In₂S₃(s), distinct color contrast in the surface potential map is also carried out (Figure 7c), exhibiting variations in the potential distribution at different positions.^[44] The value of surface potential is shown in Figure 7b, presented by the downward cyan arrow crossing over the In₂S₃(s) nanosheets. A clear -70 mV surface potential is emerged from the line profile for In₂S₃(s). However, the direct detection result delivers a relatively higher surface potential of 523 mV from the downward purple arrow crossing over the P-In₂S₃(s) nanosheets (Figure 7d). Thus, it can be concluded that the difference in surface electrostatic potential (593 mV) between In₂S₃(s) and P-In₂S₃(s) suggests the different space charge region by inducing the charge redistribution at the doped surface and bulk. This phenomenon is attributed to the In-P structure, related to the different work function. The lower surface work function in P-In₂S₃(s) could induce a built-in electric field and make the E_{F} shift to a higher energy level by the substitutional P dopants.^[41] The higher E_{F} could induce the accumulation of positive charges in the depletion region at the surface of P-In₂S₃(s), in other words, hybridized state could broaden the depletion width, which generates built-in potential and bends the band structure upward, and therefore the dynamic of hole's transfer to surface is reinforced.^[4]

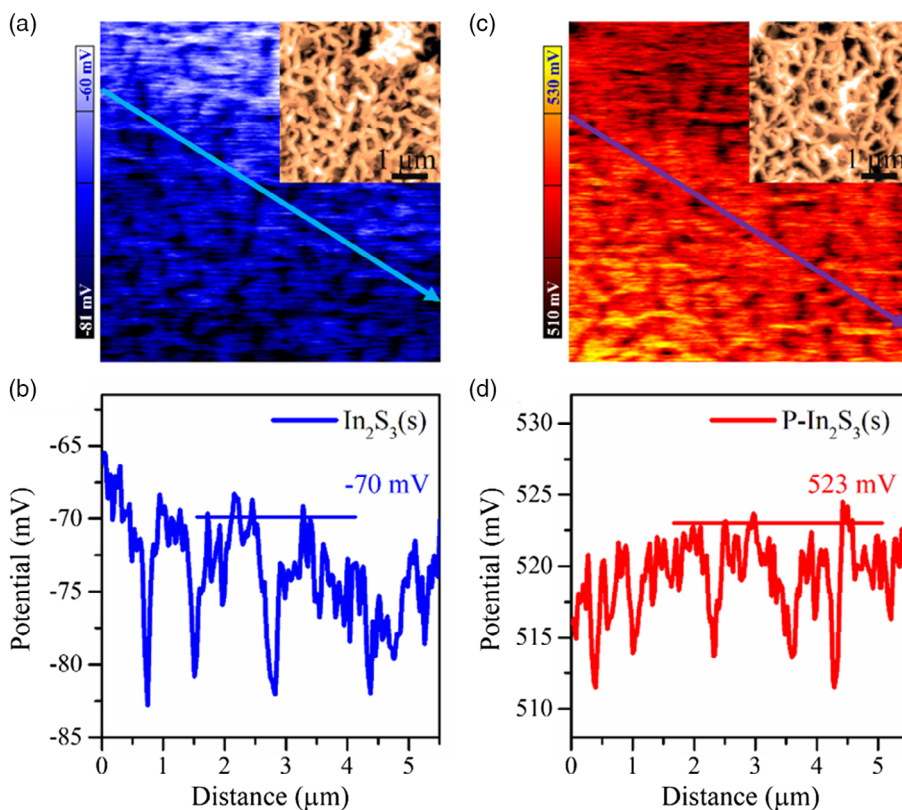


Figure 7. Surface potential of In₂S₃(s) and P-In₂S₃(s) photoanodes. a) KPFM surface potential mapping for In₂S₃(s) (inset: the corresponding topography image), and b) the detected surface potential by the downward-pointing cyan arrow as indicated in (a). c) KPFM surface potential mapping for P-In₂S₃(s) (inset: the full topography), and d) the corresponding surface potential plot taken from the locations as indicated by the downward purple arrow.

Furthermore, P-In₂S₃(s) clarifies the highest incident photo-to-electron conversion efficiencies (IPCE), which is in a good agreement with the UV-vis absorption spectra and consistent with the enhanced photocurrent (Figure 8a). After the 2 h test, the activity of P-In₂S₃(s) retains 92% of its initial photocurrent, whereas only 65% and 49% of the activity was maintained on the pristine In₂S₃(s) and In₂S₃, respectively, implying the perfect photostability after P doping (Figure 8b). The photocorrosion is suppressed because the S sites are hidden inside. The XPS spectra further illustrate the surface element ingredient and bonding structure of P-In₂S₃(s) are almost unchanged after stability test (Figure S17, Supporting Information). Herein, a possible mechanism of P substitutional doping in 2D In₂S₃ arrays for water splitting is shown in Figure 9. To verify the changes of electronic structure by P doping, the respective partial densities of states (PDOS) of In₂S₃(s) and P-In₂S₃(s) were calculated by means of DFT. For the In₂S₃(s), the valence band maximum of In₂S₃(s) is mainly composed of In 5s, In 5p, and S 3p states, and its conduction band minimum is composed by In 5s and S 3p orbitals (Figure 9a), which is in a good

agreement with literature.^[45] After P doping, the valence band of P-In₂S₃(s) is contributed by the hybridization of S 3p, P 3s, and P 3p orbitals, and the conduction band consists of In 5s, S 3p, and P 3p, showing the P doping tailors the electronic structure of host semiconductor (Figure 9b). The valence band of P-In₂S₃(s) rises due to the orbital hybridization and corroborates the M-S analysis. After the semiconductor is exposed to light, band bending immediately in the depletion region, and then facilitating the dissociation and extraction of photogenerated carriers (Figure 9c). The upshifted E_F of P-In₂S₃(s) suggests the enhanced carriers' conductivity, and the narrowed bandgap increases the light absorption. The hybridized state also prolongs carrier lifetime to promote the charge separation, increasing the concentration of holes in the valence band as well. In addition, the higher surface potential of P-In₂S₃(s) is beneficial for transferring photogenerated holes to surface where water oxidation takes place, and the board depletion region by P doping could strengthen the surface oxidation kinetics. In all, P-doping in combination with size confinement has addressed all three major problems simultaneously: tuning the electronic structure,

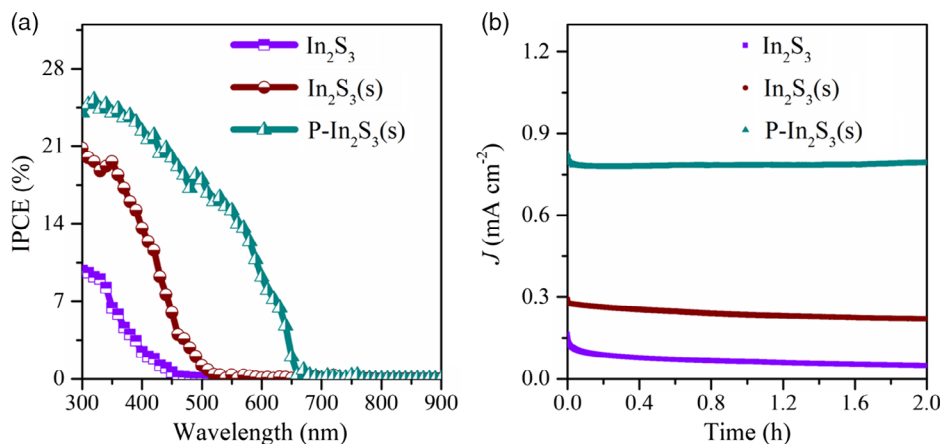


Figure 8. Overall PEC performances of as-prepared samples. a) IPCE results of various samples at 1.23 V versus RHE, and b) stability test for 2 h under AM 1.5G illumination (100 mW cm^{-2}) at 1.23 V versus RHE.

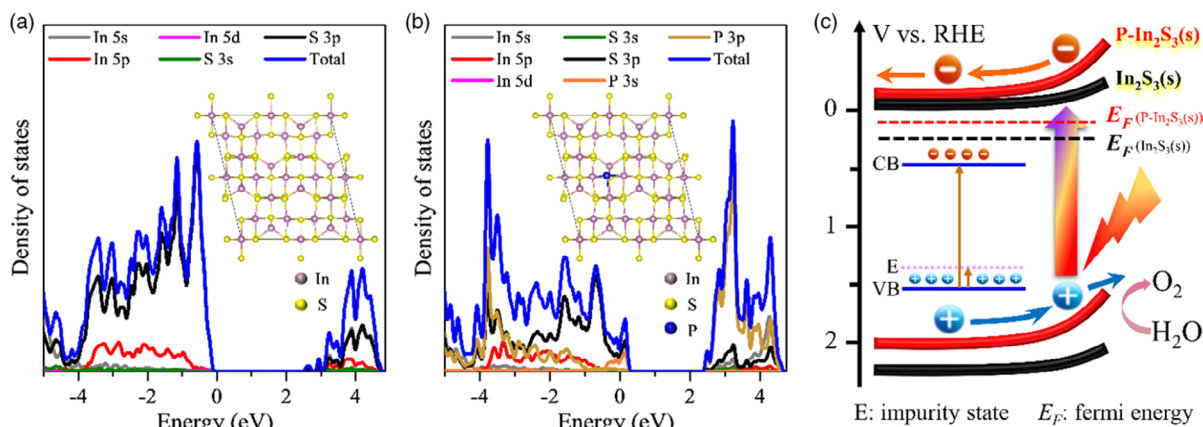


Figure 9. Mechanism for PEC water oxidation. The density of state distribution of a) In₂S₃(s) and b) P-In₂S₃(s), insets are the theoretical calculation models with slab structure. c) The proposed schematic model to illustrate the photogenerated electron-hole pairs separation and transfer pathway, the corresponding stronger energy band bending occurs in P-In₂S₃(s) photoanode for enhanced charge migration, the CB and VB is the conduction band and valence band, respectively.

suppressing charge recombination, and enhancing surface reaction kinetics, this strategy may be further explored in solar energy conversion devices.

3. Conclusions

An integrated 2D P-In₂S₃(s) arrays was fabricated by three-steps: preseeding by SILAR, solvothermal, and phosphating method. With seed-mediated growth, the nucleation barrier is significantly lowered by the nanoparticles in a heterogeneous nucleation process and the In₂S₃(s) nanosheets were regulated to a much smaller size, demonstrated large specific surface area with more active sites. By phosphorization, DFT calculation showed that the hybridization of P 3s, P 3p, and S 3p formed impurity states near the valence band of In₂S₃, and changed the electronic structure of host semiconductor. The hybridization of In–P structure was conducive to prolong the carrier lifetime, reduce the recombination of charges, and enhance the carriers' concentration. The energetic surface state of P-In₂S₃(s) with broad depletion width promoted the transfer speed of photogenerated holes to surface for water oxidation. Combined the size confinement and P-doping in 2D structure, P-In₂S₃(s) presented a 5.3-fold enhancement in photocurrent density compared with pristine In₂S₃, and the highly charge separation efficiency (40%) and oxidation kinetics (79%).

4. Experimental Section

Preparation of 2D In₂S₃ Arrays: 2D In₂S₃ arrays were synthesized by a solvothermal procedure. About 16 mmol InCl₃ and 24 mmol thioacetamide were dissolved in 30 ml ethylene glycol solution and vigorously stirred for 10 min at room temperature. Subsequently, the clear solution was transferred to a Teflon-lined stainless steel autoclave, to which the FTO substrate was placed with the conductive side down against the wall at an angle of ≈30°, and then placed inside an oven at 180 °C for 2 h. After the reaction, the system was cooled down to room temperature naturally, a yellow film on the FTO substrate was formed. After washing the product by deionized water and ethyl alcohol repeatedly, followed by a thermal annealing at 300 °C for 1 h to improve its crystallinity, the 2D In₂S₃ arrays were synthesized.

Preparation of Small-sized 2D In₂S₃ Arrays (In₂S₃(s)): The In₂S₃(s) was synthesized by two steps. First, SILAR was used to grow the In₂S₃ seed layer on the FTO surface. The seed crystal growth by SILAR technique was a solution phase method to grow thin films at room temperature and ambient pressure. The cation and anion constituents of film material are adsorbed on the surface of the substrate in turn from different precursor solutions. In detail, the pretreated FTO substrate was immersed vertically in 25 mM InCl₃ aqueous solution (30 mL) for 1 min at room temperature and In ions were adsorbed on the substrate due to attractive forces between the ions and the substrate. Then, the air-dried film was vertically transferred to 36.5 mM Na₂S aqueous solution (30 mL) kept at 35 °C for 1 min to adsorb S ions, and finally the film was immersed into deionized water for 5 s to remove the excess S ions and further dried in air for 30 s. Here, the surface coagulation occurs around these nucleation sites. After repeating several times of this SILAR cycles, the In₂S₃ seed layer was obtained. An appropriate uniform seed layer was obtained by repeating 8 SILAR cycles. As a second step, the seed layer was placed into a mixed solution for growth of smaller-sized 2D In₂S₃(s) by solvothermal method in 16 mmol InCl₃ and 24 mmol thioacetamide. The FTO substrate with In₂S₃ seed layer was placed into the solution, and the surface was faced down with an inclination against the wall of autoclave. After transferring it into oven at 180 °C for 2 h and cooling down to room

temperature, the small-sized In₂S₃(s) arrays were obtained successfully. In the solvothermal reaction, the seed layer by SILAR decreased the surface energy of the substrate and reduced the size of In₂S₃ nanosheets by aid of heterogeneous nucleation process.

Preparation of P Doped In₂S₃(s) Arrays (P-In₂S₃(s)): Briefly, a simple chemical vapor deposition (CVD) method was used to phosphorize 2D In₂S₃(s) arrays using a tube furnace. About 0.15 g NaH₂PO₂ was placed in the tube furnace, whereas In₂S₃(s) film was placed at a back position ≈5 cm. Subsequently, the tube furnace was annealed at 300 °C for several minutes with a heating rate of 2 °C min⁻¹ under Ar flow. Phosphine (PH₃) was decomposed from NaH₂PO₂ and acts as the resource of P dopants. When the temperature cooled down to room temperature, the P-doped In₂S₃(s) was obtained successfully. These P-In₂S₃(s) samples with various doping amounts are related to the phosphating time, which are listed in Table S1, Supporting Information, and detected by the ICP technique.

Theoretical Methods: First principle DFT calculations were carried out by Vienna Ab initio Simulation Package (VASP) with the projector augmented wave (PAW) method. The exchange-functional is treated using the GGA of Perdew–Burke–Ernzerhof (PBE) functional. The cut-off energy of the plane-wave basis is set at 450 eV to optimize calculations of atoms and cell optimization. The Brillouin zone integration is carried out using 3 × 3 × 3 Monkhorst–Pack k-point sampling for a primitive cell. The self-consistent calculations apply a convergence energy threshold of 10⁻⁵ eV. The equilibrium lattice constants are optimized with maximum stress on each atom within 0.05 eV Å⁻¹. The Hubbard U (DFT + U) corrections for 3d-transition metal.

Supporting Information

Supporting Information is available from the Wiley Online Library or from the author.

Acknowledgements

This work was supported by Graduate Research and Innovation Foundation of Chongqing, China (Grant No. CYS18050), the Fundamental Research Funds for the Central Universities (2018CDJDWL0011), and the Projects of President Foundation of Chongqing University (2019CDXZWL002).

Conflict of Interest

The authors declare no conflict of interest.

Keywords

2D In₂S₃, electronic structures, P doping, photoelectrochemical systems, seed layers

Received: October 1, 2020

Revised: October 30, 2020

Published online: November 25, 2020

- [1] J. H. Kim, J. H. Kim, J. H. Kim, Y. K. Kim, J. S. Lee, *Sol. RRL* **2019**, *4*, 1900328.
- [2] B. Tang, Z. G. Yu, Y. Zhang, C. Tang, H. L. Seng, Z. W. Seh, Y.-W. Zhang, S. J. Pennycook, H. Gong, W. Yang, *J. Mater. Chem. A* **2019**, *7*, 13339.
- [3] Z. Wang, T. D. Nguyen, L. P. Yeo, C. K. Tan, L. Gan, A. Y. Tok, *Small* **2020**, *16*, 1905826.

- [4] L. Yang, S. K. Ravi, D. K. Nandakumar, F. I. Alzakia, W. Lu, Y. Zhang, J. Yang, Q. Zhang, X. Zhang, S. C. Tan, *Adv. Mater.* **2019**, *31*, 1902963.
- [5] L. Yang, Y. Xiong, P. Xiao, Y. Zhang, *Electrochim. Acta* **2019**, *307*, 43.
- [6] K. Zhang, J. Liu, L. Wang, B. Jin, X. Yang, S. Zhang, J. H. Park, *J. Am. Chem. Soc.* **2020**, *142*, 8641.
- [7] E. Ghorbani, K. Albe, *Phys. Rev. B* **2018**, *98*, 205201.
- [8] W. Tian, C. Chen, L. Meng, W. Xu, F. Cao, L. Li, *Adv. Energy Mater.* **2020**, *10*, 1903951.
- [9] M. Bianchini, J. Wang, R. J. Clément, B. Ouyang, P. Xiao, D. Kitchaev, T. Shi, Y. Zhang, Y. Wang, H. Kim, M. Zhang, J. Bai, F. Wang, W. Sun, G. Ceder, *Nat. Mater.* **2020**, *19*, 1088.
- [10] J. Piella, N. G. Bastús, V. Puentes, *Chem. Mater.* **2016**, *28*, 1066.
- [11] W. Huang, L. Gan, H. Yang, N. Zhou, R. Wang, W. Wu, H. Li, Y. Ma, H. Zeng, T. Zhai, *Adv. Funct. Mater.* **2017**, *27*, 1702448.
- [12] W. Sun, D. A. Kitchaev, D. Kramer, G. Ceder, *Nat. Commun.* **2019**, *10*, 573.
- [13] D. Zhou, H. Shu, C. Hu, L. Jiang, P. Liang, X. Chen, *Cryst. Growth Des.* **2018**, *18*, 1012.
- [14] B. Tang, Z. G. Yu, L. Huang, J. Chai, S. L. Wong, J. Deng, W. Yang, H. Gong, *ACS Nano* **2018**, *12*, 2506.
- [15] H. Han, S. Kment, F. Karlicky, L. Wang, A. Naldoni, P. Schmuki, R. Zboril, *Small* **2018**, *14*, 1703860.
- [16] J. Liu, X. Liu, Z. Chen, L. Miao, X. Liu, B. Li, L. Tang, K. Chen, Y. Liu, J. Li, Z. Wei, X. Duan, *Nano Res.* **2019**, *12*, 463.
- [17] V. Andrei, B. Reuillard, E. Reisner, *Nat. Mater.* **2020**, *19*, 189.
- [18] Y. Xiong, L. Yang, L. Li, L. Peng, Y. Liu, R. Luo, X. Wei, P. Xiao, H. He, *ACS Appl. Energy Mater.* **2019**, *2*, 6780.
- [19] J. H. Baek, T. M. Gill, H. Abroshan, S. Park, X. Shi, J. Nørskov, H. S. Jung, S. Siahrostami, X. Zheng, *ACS Energy Lett.* **2019**, *4*, 720.
- [20] R. Shi, H. F. Ye, F. Liang, Z. Wang, K. Li, Y. Weng, Z. Lin, W.-F. Fu, C.-M. Che, Y. Chen, *Adv. Mater.* **2018**, *30*, 1705941.
- [21] C. G. Tang, M. N. Syafiqah, Q.-M. Koh, C. Zhao, J. Zaini, Q.-J. Seah, M. J. Cass, M. J. Humphries, I. Grizzi, J. H. Burroughes, R.-Q. Png, L.-L. Chua, P. K. H. Ho, *Nature* **2019**, *573*, 519.
- [22] T. Zhang, K. Fujisawa, F. Zhang, M. Liu, M. C. Lucking, R. N. Gontijo, Y. Lei, H. Liu, K. Crust, T. Granzier-Nakajima, H. Terrones, A. L. Elias, M. Terrone, *ACS Nano* **2020**, *14*, 4326.
- [23] J. Suh, T. L. Tan, W. Zhao, J. Park, D.-Y. Lin, T.-E. Park, J. Kim, C. Jin, N. Saigal, S. Ghosh, Z. M. Wong, Y. Chen, F. Wang, W. Walukiewicz, G. Eda, J. Wu, *Nat. Commun.* **2018**, *9*, 199.
- [24] K. Zhang, B. M. Bersch, J. Joshi, R. Addou, C. R. Cormier, C. Zhang, K. Xu, N. C. Briggs, K. Wang, S. Subramanian, K. Cho, S. Fullerton-Shirey, R. M. Wallace, P. M. Vora, J. A. Robinson, *Adv. Funct. Mater.* **2018**, *28*, 1706950.
- [25] R. J. Britto, J. D. Benck, J. L. Young, C. Hahn, T. G. Deutsch, T. F. Jaramillo, *J. Phys. Chem. Lett.* **2016**, *7*, 2044.
- [26] Q. Yang, J. Du, J. Li, Y. Wu, Y. Zhou, Y. Yang, D. Yang, H. He, *ACS Appl. Mater. Interfaces* **2020**, *12*, 11625.
- [27] E. Hua, S. Jin, X. Wang, S. Ni, G. Liu, X. Xu, *Appl. Catal., B* **2019**, *245*, 733.
- [28] X. Jin, J. Li, Y. Cui, X. Liu, X. Zhang, J. Yao, B. Liu, *Inorg. Chem.* **2019**, *58*, 11630.
- [29] X. Bu, Y. Gao, S. Zhang, Y. Tian, *Chem. Eng. J.* **2019**, *355*, 910.
- [30] S. Li, L. Wang, Y. Li, L. Zhang, A. Wang, N. Xiao, Y. Gao, N. Li, W. Song, L. Ge, J. Liu, *Appl. Catal., B* **2019**, *254*, 145.
- [31] M. Li, L. Chen, C. Zhou, C. Jin, Y. Su, Y. Zhang, *Nanoscale* **2019**, *11*, 18071.
- [32] B. Asenjo, C. Guillén, A. M. Chaparro, E. Saucedo, V. Bermudez, D. Lincot, J. Herreroa, M. T. Gutiérrez, *J. Phys. Chem. Solid* **2010**, *71*, 1629.
- [33] D. H. Guan, X. X. Wang, M. L. Li, F. Li, L. J. Zheng, X. L. Huang, J. J. Xu, *Angew. Chem., Int. Ed.* **2020**, *59*, 2.
- [34] H. Huang, B. Dai, W. Wang, C. Lu, J. Kou, Y. Ni, L. Wang, Z. Xu, *Nano Lett.* **2017**, *17*, 3803.
- [35] L. Wang, L. Xia, Y. Wu, Y. Tian, *ACS Sustainable Chem. Eng.* **2016**, *4*, 2606.
- [36] Y. Xiong, L. Yang, D. K. Nandakumar, Y. Yang, H. Dong, X. Ji, P. Xiao, S. C. Tan, *J. Mater. Chem. A* **2020**, *8*, 5612.
- [37] B. Yang, M. Wang, X. Hu, T. Zhou, Z. Zang, *Nano Energy* **2019**, *57*, 718.
- [38] L. Yang, Y. Xiong, L. Li, Y. Yang, D. Gao, L. Liu, H. Dong, P. Xiao, Y. Zhang, *ACS Appl. Energy Mater.* **2018**, *1*, 4591.
- [39] J. V. Patil, S. S. Mali, C. K. Hong, *Sol. RRL* **2020**, *4*, 2000164.
- [40] H. Fang, J. Yang, S. Adjokatse, E. Tekelenburg, M. E. Kamrninga, H. Duim, J. Ye, G. R. Blake, J. Even, M. A. Loi, *Adv. Funct. Mater.* **2020**, *30*, 1907979.
- [41] L. Yang, D. K. Nandakumar, L. Miao, L. Suresh, D. Zhang, T. Xiong, J. V. Vaghasiya, K. C. Kwon, S. C. Tan, *Joule* **2020**, *4*, 176.
- [42] L. M. Peter, K. G. U. Wijayantha, A. A. Tahir, *Faraday Discuss.* **2012**, *155*, 309.
- [43] L. Guo, P. S. Shinde, Y. Ma, L. Li, S. Pan, F. Yan, *Sol. RRL* **2020**, *4*, 1900442.
- [44] L. Yang, L. Loh, D. K. Nandakumar, W. Lu, M. Gao, X. L. C. Wee, K. Zeng, M. Bosman, S. C. Tan, *Adv. Mater.* **2020**, *32*, 2000971.
- [45] Z. Zhao, J. Yi, D. Zhou, *Comp. Mater. Sci.* **2013**, *73*, 139.